INVESTIGATION ON THE SOLID-LIQUID FLOW IN THE REAR CHAMBER OF A SUBMERSIBLE MULTI-STAGE SLURRY PUMP

Bo Hu, Friedrich-Karl Benra, Weigang Lu

Department of Mechanical Engineering,
University of Duisburg-Essen,
47057 Duisburg,
Germany,
E-mail: bo.hu.1987@stud.uni-due.de

ABSTRACT

The complicated solid-liquid flow in a grooved rotating cavity is strongly influenced by both axial and radial gaps. This paper presents a numerical study on the influences of both axial and radial gaps on the solid-liquid flow inside the grooved rear chambers, aiming to accomplish effective micro-sized sand exclusion. The commercial RANS solver CFX 14.0 is used to predict the movements of dispersed phase in six rear chambers. The simulation results show that the periphery flow has little influence on the cavity flow when the dimensionless radial gap is no more than 0.038. Although the flow near the groove is turbulent and the cavity is open, Batchelor type flow can be predicted in most parts of all of the six cavities. The dimensionless tangential velocity of slurry increases with the decrease of axial gap, which contribute to better sand discharge capacity. Experimental abrasion investigations show that the simulation results are reasonable and the service life of SMSP is dramatically improved.

NOMENCLATURE

a	axial coordinate of monitor plane
A	axial gap between disk and wall
Ats	accumulated time step
b_2	blade outlet width
c	suitable dimensionless radial gap
C	suitable radial gap
D_1	impeller inlet diameter
D_2	impeller outer diameter
Ek	Ekman Number
G	dimensionless gap width
H	pressure head
n	speed of rotation
N_{cg}	grid number of cavity
n_s	specific speed
P	pump power
p_0	pressure at pump outlet when t=0
p_T	pressure at pump outlet when t=T
p^*	pressure ratio of p_T to p_0
Δr	dimensionless radial gap
Q	flow rate
R	outer radius of the disk
Re_φ	circumferential Reynolds Number
ΔR	radial gap
SMSPs	submersible multi-stage slurry pumps
t	time
v_r	dimensionless radial velocity
v_{rw}	radial velocity in wall layer
v_{rd}	radial velocity in disk layer
v_θ	dimensionless tangential velocity
$v_{\theta 1}$	v_θ at monitor point 1
$v_{\varphi w}$	tangential velocity in wall layer
$v_{\varphi d}$	tangential velocity in disk layer
X	radial gap of rear chamber No.1
Z	aixal gap of rear chamber No.1
β_2	blade outlet angle
δ_w	thickness of the wall layer
δ_d	thickness of the disk layer
η	pump efficiency
θ	blade wrapping angle
λ	the ratio of ΔR to A
φ_s	solid volume fraction
Ω	angular speed of the disk

INTRODUCTION

The mechanical seals of submersible multi-stage slurry pumps (SMSPs) are fragile. In most of

the coal mines, the maximum size of sand is less than 0.1mm, which enters the mechanical seal easily. Batchelor (1951) noticed the presence of wall layer and disk layer, which are separated by a core of fluid. Daily and Nece (1960) distinguished four different flow regimes based on circumferential Reynolds Number Re_φ and dimensionless gap width G. Kurokawa et al. (1988) discussed the flow in the side gap of an impeller. His theoretical results are supported by measurements. This flow model, which is widely used in the industry and is based on the assumption of the flow regime IV with core region and two boundary layers (three-layer-model). Randiamampianina et al. (1997) observed that laminar and turbulent flows coexist inside the cavity. Djaoui et al. (1998) investigated the influence of peripheral conditions on the flow pattern in an open cavity without superimposed flow. They found that a dimensionless parameter λ has a great influence on the flow structure inside the cavity. D'Haudt et al. (2006) accomplished both numerical and experimental studies of the flow in rotating disk systems. They pointed out that Batchelor type flow can be observed even if the cavity is open and the disk is not infinite. Debuchy et al. (2009) found that the fluid was expelled radially by the rotating disk and replaced both by reinjection of the expelled and ambient fluid. Will et al. (2010) investigated the flow in the side chambers of a centrifugal pump. The rear chamber of SMSP is selected as research model, shown in Figure 1(a). Based on above studies, the possible flow patterns in the rear chamber of SMSP are shown in Figure 1(b).

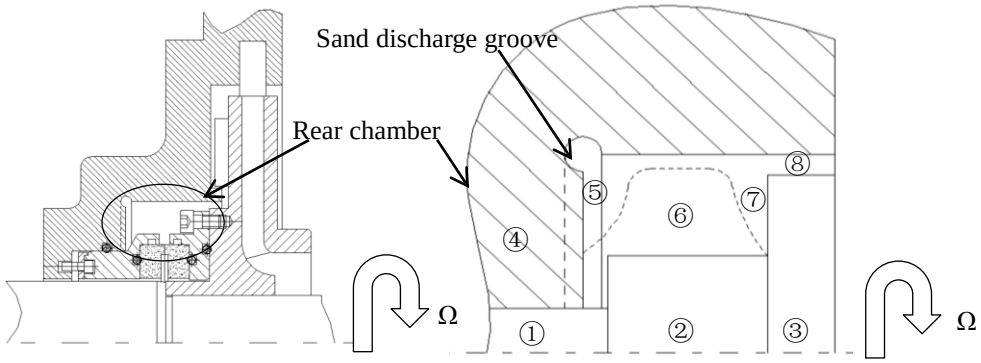

①: Shaft; ②: Shaft shoulder; ③: Disk; ④: Stator; ⑤: Wall layer; ⑥: Core; ⑦: Disk layer; ⑧: ΔR

(a) Rear chamber of SMSP (b) Possible flow patterns in the rear chamber

Fig. 1: **Geometries and possible flow patterns inside the rear chamber of SMSP**

Since the micro-sized sand moves with the conveying fluid (Hazra and Steiner, 2007), the flow patterns of the solid-liquid flow with micro-sized sand may be similar to that of the pure water. Due to mass conservation, an axial convection of fluid from the outer radius of disk to that of the stator takes place. A sand discharge groove, shown in Figure 2(a), is designed based on that axial convection.

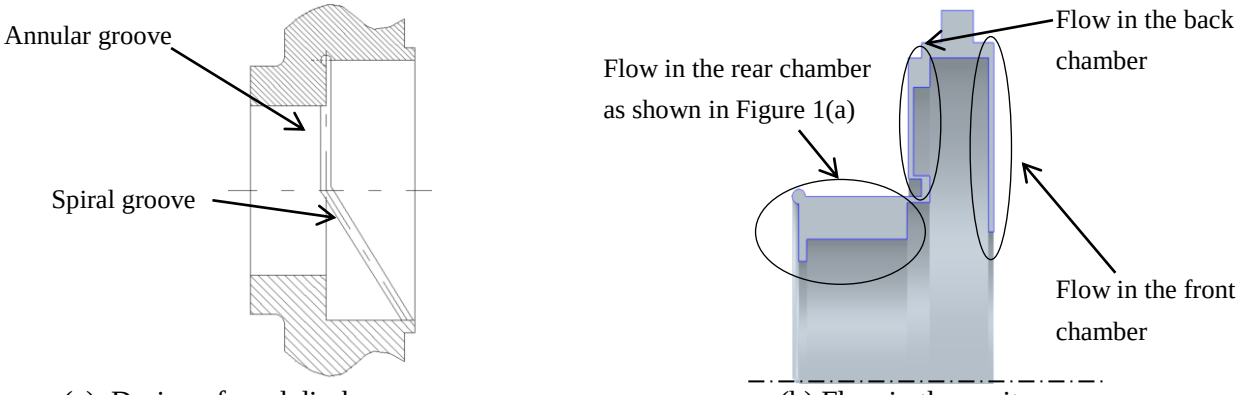

(a) Design of sand discharge groove (b) Flow in the cavity

Fig. 2: **Cavity with sand discharge groove**

The groove includes two parts: an annular groove at the outer radius of stator and a spiral groove on the inner surface of the stator, as shown in Figure 2(a). The flow in the cavity is shown in Figure 2(b). Due to the axial convection of slurry, sand may enter the annular groove before moving towards the shaft. With large tangential velocities, sand may be discharged out of the rear chamber along the spiral groove. In this study, the commercial CFX 14.0 is used to predict the solid-liquid flow in 6 grooved rear chambers. This paper focuses on selecting optimum parameters of both axial and radial gaps to improve sand discharge capacity.

GEOMETRICAL PARAMETERS

Main geometry parameters of the impeller are given in Table 1.

$\beta_2(^o)$	D_2 (mm)	D_1 (mm)	b_2 (mm)	$\theta(^o)$	n(1/min)	n_s (n_s=3.65$\frac{n\sqrt{Q}}{H^{3/4}}$)
23	220	80	10	130	2900	42

Table 1: **Main geometry parameters of the impeller**

Five dimensionless parameters, namely G, Δr, Re, Ek and λ, are used to distinguish the different flow patterns in the 6 rear chambers. They are respectively defined by:.

$$G = \frac{A}{R};\ \Delta r = \frac{\Delta R}{R};\ Re_{\varphi} = \frac{\Omega R^2}{\upsilon};\ Ek = \frac{1}{G^2 Re};\ \lambda = \frac{\Delta R}{A} \tag{1}$$

When G<<1, Re>>1 and Ek<<1, the inertia effects are dominant and the flow is turbulent. When the axial gap is too wide, sand is more likely to move towards the shaft before entering the groove. At the same time, periphery flow will dramatically influence the cavity flow unless the dimensionless radial gap, noted as Δr, drops below a certain value (D'Haudt et al. 2009). Hence, G and Δr should be decreased. 6 cavities are designed based on above principles. Their rear chambers are noted from No.1 to No.6, shown in Figure 3. The values of axial and radial gaps of No.1, noted as Z and X, are 24 mm and 3 mm, respectively. The outer radius of the disk, noted as R, is 60 mm.

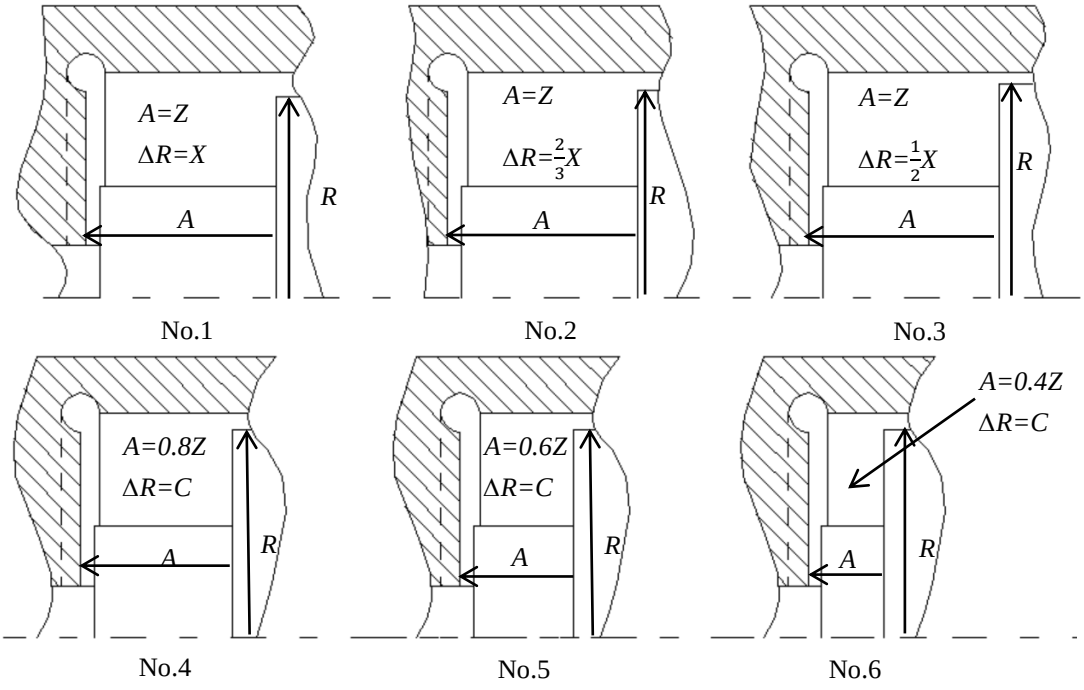

Figure 3: **Geometries of rear chambers**

The first three chambers are designed to find the suitable value of the radial gap. The radial gap of the No.4, No.5 and No.6 will be designed based on that value, noted as *C*. The suitable dimensionless radial gap is noted as *c*. The values of *G* are minimized from No.4 to No.6 to increase the amount of sand which is expelled into the groove. According to the values of the dimensionless parameters, given in Table 2, the flow regimes in all the cavities are flow regime IV, shown in Figure 4. In this study, the diameter and the lead of the spiral groove are 5 mm and 85 mm, respectively. The diameter of the annular groove is 5 mm.

Cavities	Δr	G	R_e	E_k	λ
No.1	0.050	0.4	0.87×10^6~1.2×10^6	5.5×10^{-6}	0.125
No.2	0.038				0.08
No.3	0.025				0.06
No.4	c	0.32		8.6×10^{-6}	0.10
No.5		0.24		1.5×10^{-5}	0.14
No.6		0.16		3.4×10^{-5}	0.21

Table 2: **Values of dimensionless parameters of the rear chambers**

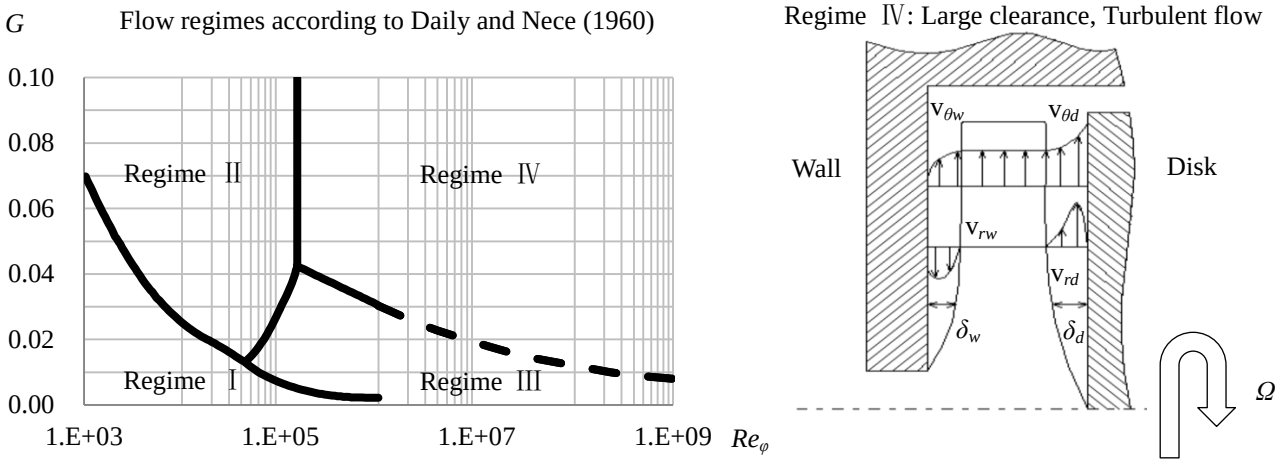

Figure 4：**Flow regimes and flow patterns in all the cavities**

NUMERICAL SIMULATION

Flow domains and types of interfaces for numerical simulation are given in Figure 5. The flow domains include four parts: inlet, impeller, cavity with rear chamber and volute with two outlets. The analysis type is set as steady state. The simulation is carried out using Multiple Frames of reference methods. 3D simulation is conducted with a commercial Ansys CFX 14.0 solver. As shown in Figure 6, the meshes of the cavity with both rear chamber and spiral groove are generated with hybrid grids. The other parts are generated with structured grids. Standard *k-ε* model is used to predict the turbulent flow. All the particles in the cavities are considered to have a spherical shape. The movement of particles is predicted with zero equation. Schiller-Naumann drag model is used to calculate the drag force. The lift force of particles is calculated with Saffman-Mei lift force model. Both turbulent dispersion force and wall lubrication force between particles and wall are ignored during the simulation. Instead of resolving boundary layers, scalable wall functions are used to model the viscous effects in the near wall regions. The temperature of slurry is set as 20℃. Since the volute has two outlets, noted as outlet 1 and outlet 2 (shown in Figure 5), the flow rates through the two outlets are considered as an equal value. Based on the design requirements, the values of

mass flow rate at inlet, pressure at outlet and solid volume fraction are set as 5.4 kg/s, 2.6 MPa and 10%, respectively. The surface roughness value of all the domains is 12.5 μm. The speed of rotation interface between rotatable parts and liquid is 2900/min.

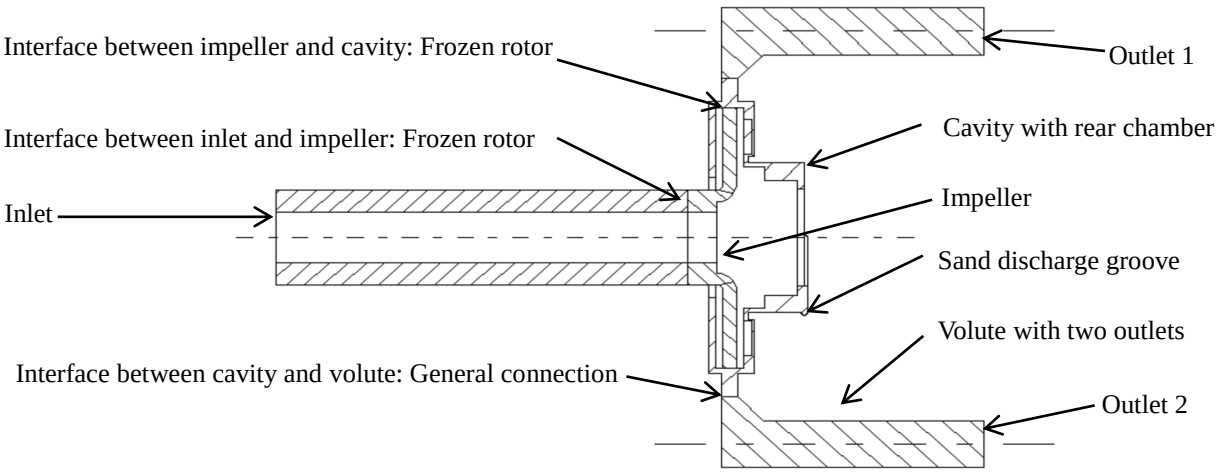

Figure 5: **Flow domains and types of interfaces for numerical simulation**

Impeller

Volute with two outlets

Inlet

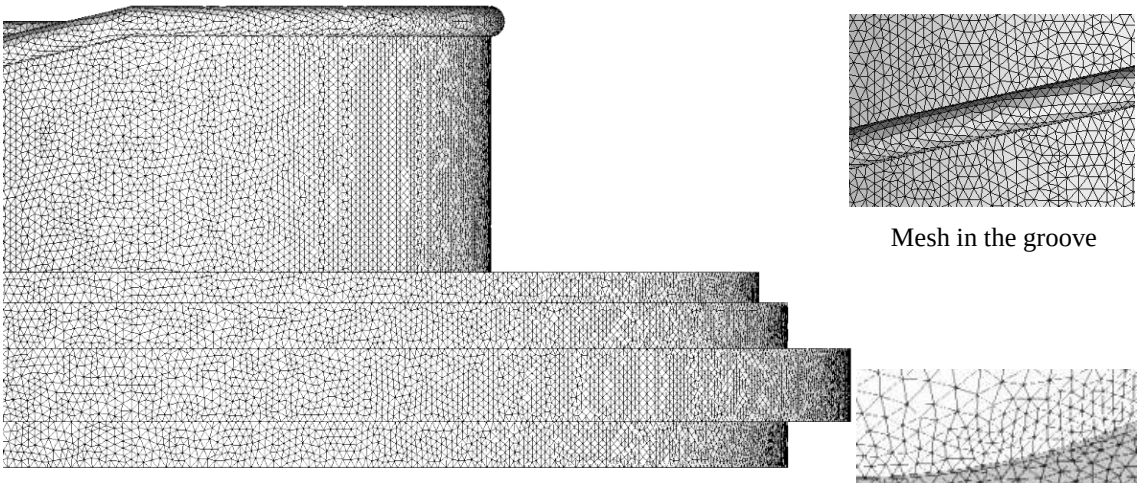

Cavity with sand discharge groove

Mesh in the groove

Mesh near the radial gap

Figure 6: **Mesh of fluid domains**

The locations of monitor points are shown in Figure 7.

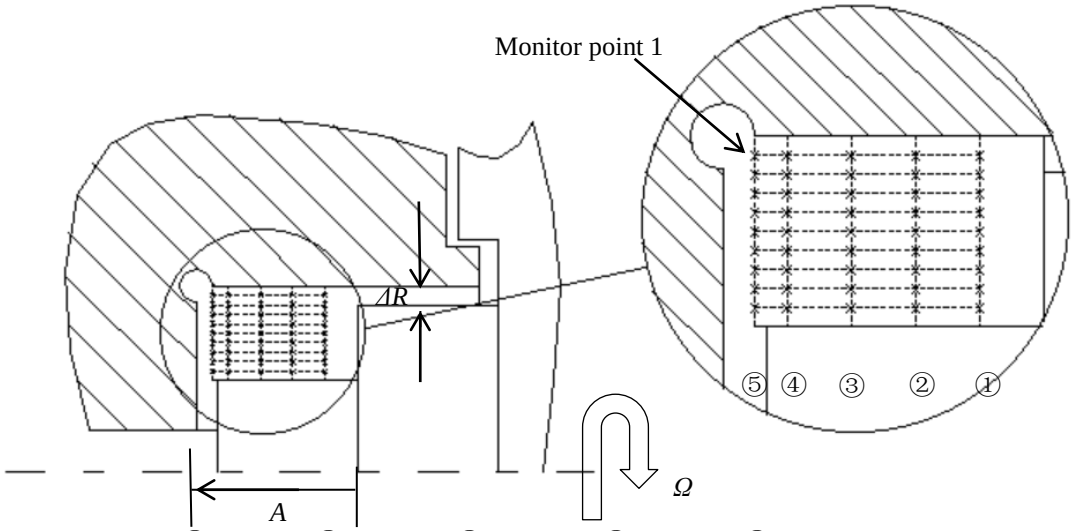

①: a=0.2A; ②: a=0.4A; ③: a=0.6A; ④: a=0.8A; ⑤: a=0.9A

Figure 7: **Arrangement of monitor points in the rear chamber**

The convergence criteria of all the simulations is set as 10^{-5}. The dimensionless tangential velocity at monitor point 1 (shown in Figure 7) is noted as $v_{\theta 1}$. The analyses are considered to be converged, verified by the scaled residuals for all the equations drop below 10^{-5} and the convergence history of $v_{\theta 1}$ in No.1, shown in Figure 8. The simulation for all the cavities share almost the same convergence behaviors.

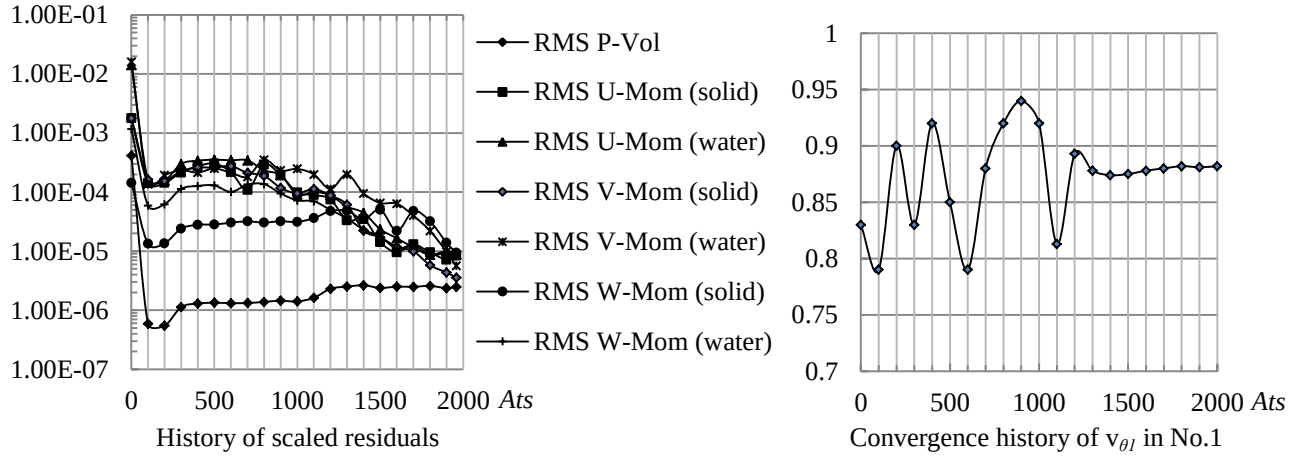

Figure 8: **Convergence behavior of simulation for No.1**

In former studies, the mesh independent studies for impeller and volute have been accomplished. Hence, only the mesh independent study of the cavity is performed, shown in Figure 9.

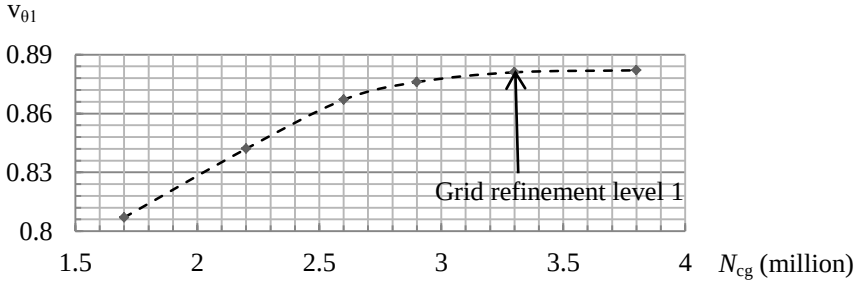

Figure 9: **Mesh sensitive analysis**

Both axial and radial gaps of No.1 are larger than the other chambers. Hence, the grid number for cavity 1 is also suitable for the other chambers. According to the results, the total grid number of the cavities, noted as N_{cg}, should exceed 3.5 millions. The grid refinement level is level 1. The y^+ values range from 30.6 to 78, which are in the valid range of scalable wall functions.

RESULTS AND DISCUSION

In this section, experimental data and simulation results are presented in order to analyze the sand discharge capacity. All the velocities have been made dimensionless by dividing $\Omega \cdot R$.

Selecting Suitable Radial Gap

The distributions of dimensionless radial velocity, noted as v_r, are shown in Figure 10. The results in No.1, No.2 and No.3 are presented to select the suitable radial gap.

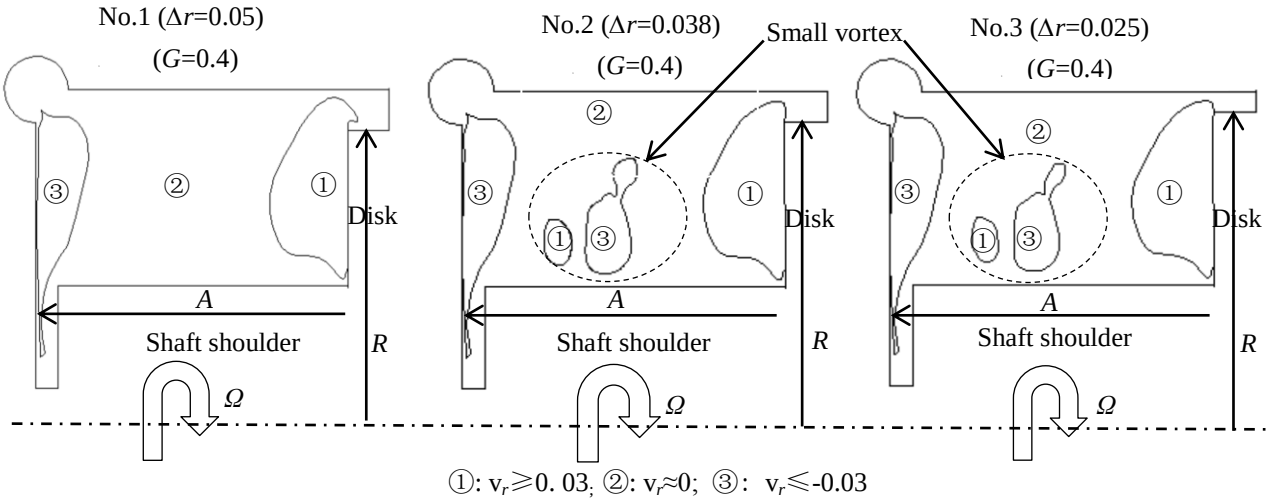

Figure 10: **Distributions of radial velocity**

The positive and negative values of v_r indicate radial outward flow and radial inward flow, respectively. Both the wall layer (where $v_r \leqslant -0.03$) and the disk layer (where $v_r \geqslant 0.03$) can be predicted inside of the three cavities.

The values of v_r are close to zero in most of the cavities, which indicate that each of the three cavities has a central core.

The simulation results show that when Δr decreses to 0.038 (shown in No.2, Figure 10)，a small vortex near the shaft shoulder occurs. The vortex almost remains the same when Δr decreases further to 0.025 (shown in No.2, Figure 10). It indicates that the periphery flow has little influence on the cavity flow when $\Delta r \leqslant 0.038$. Considering the shaft deformation, Δr =0.025 is not selected as optimal value. Hence, the Δr of No.4, No.5 and No.6 is selected as 0.038.

Movement of Particles on the Meridian Plane

Since Δr has been found, the movements of particles on the meridian plane are predicted to analyze the influence of the axial gap on the cavity flow. The distributions of streamlines on the meridian plane are shown in Figure 11. The movements of sand are shown by the directions of arrows. The flow near the groove is turbulent. In cavity 2, most of the sand rotates in the chamber and moves towards the shaft before entering the groove. Only a small portion of sand enters the groove. From the simulation results of No.2, No.4 and No.5, it seems that the amount of sand entering the groove increases with the decrease of axial gap in general. The cavity flow is similar to Batchelor type flow. The movements of slurry are turbulent near the groove and shaft shoulder in No.6. Some particles move out of the groove towards the shaft in No.6. It seems that when G decreases further from 0.24 to 0.16, the shaft shoulder and groove contribute to more turbulent flow, which may lower the sand discharge capacity.

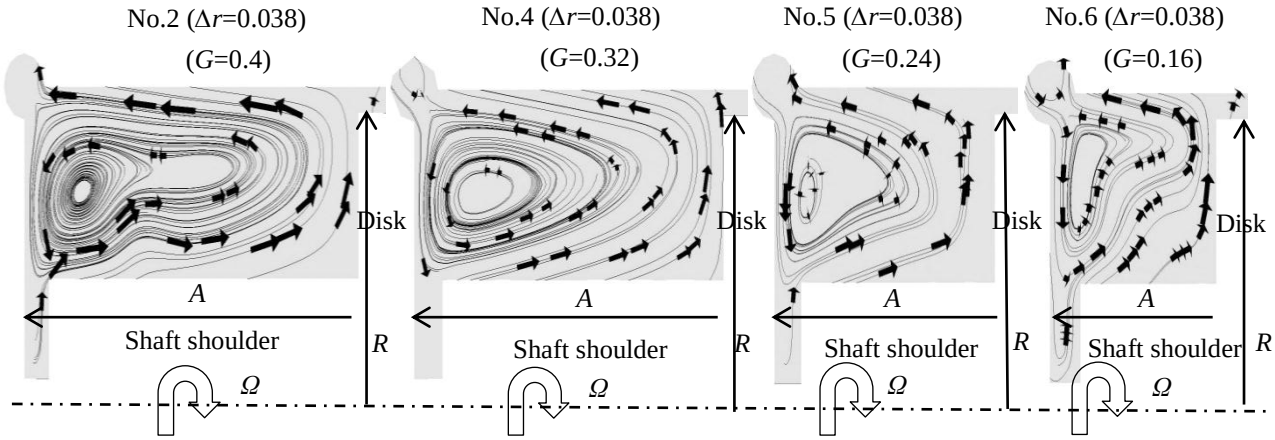

Figure 11: **Movement of particles on the meridian plane**

Distribution of Dimensionless Radial Velocity

The distributions of dimensionless radial velocity, noted as v_r, are shown in Figure 12. The positive and negative values represent radial outward flow and radial inward flow, respectively.

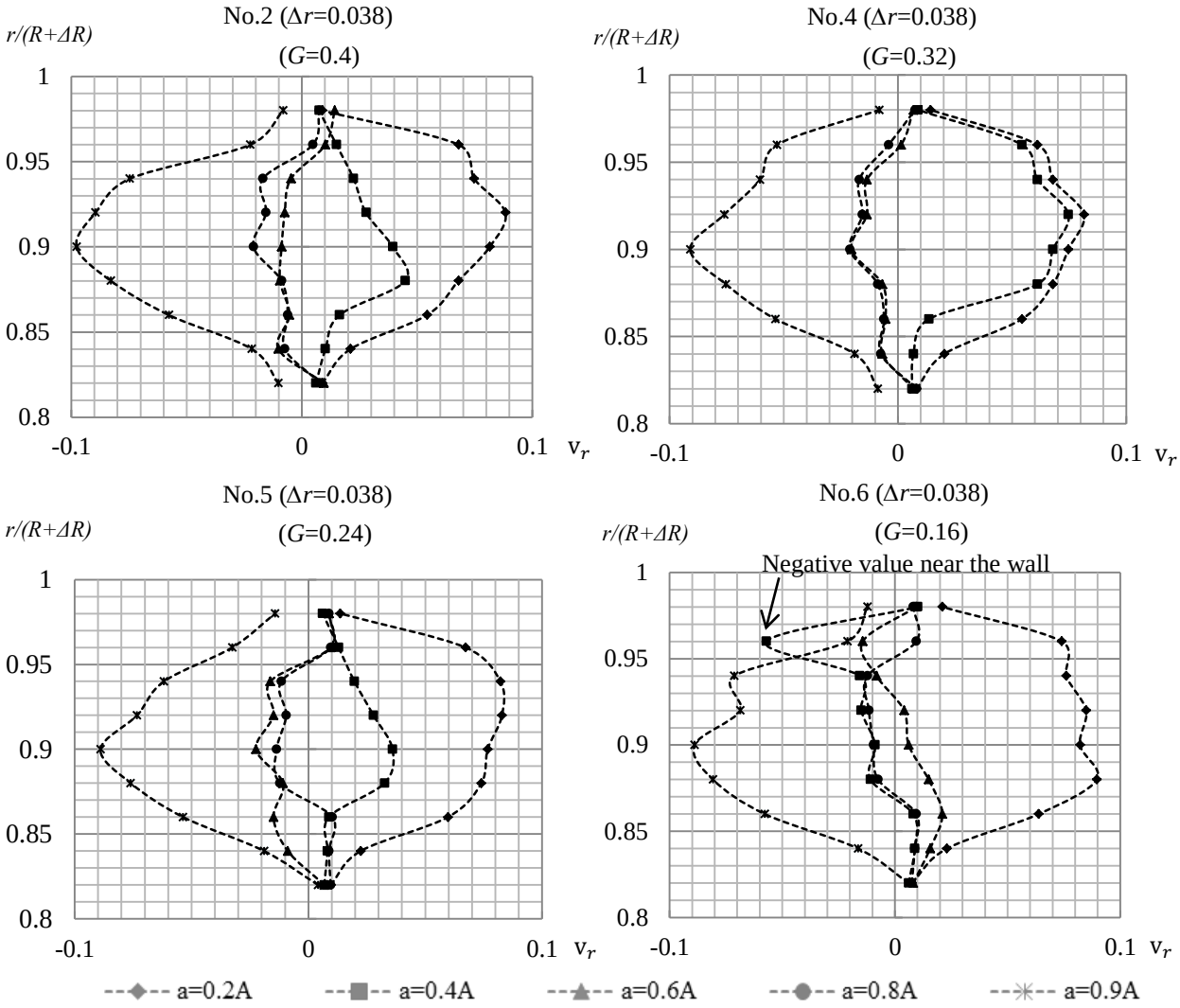

Figure 12: **Distributions of dimensionless radial velocity**

The results reveal that there is a central core ($v_r \approx 0$) between the wall layer ($v_r \leq -0.05$) and the disk layer ($v_r \geq 0.05$) in each cavity. Although the cavity is open the disk is not infinite, Batchelor type flows can be predicted in all of the rear chambers.

On a=0.2A plane and a=0.9A plane (shown in Figure 7), the values of v_r drop obviously with the increase of radius after reaching their peaks.

On *a*=0.4*A* plane (shown in Figure 7) of No.4, most the values of v_r exceed 0.05. This may indicate that most of the monitor points on a=0.4*A* plane are in the dick layer in No.4.

In No.6, the negative values of v_r near the wall on the *a*=0.4*A* plane indicate that the flow move towards the shaft. One reason may be that the influences of spiral groove and shoulder on the fluid are strong at that axial gap.

Distributions of Dimensionless Tangential Velocity

The simulation results of dimensionless tangential velocity, noted as v_θ, are shown in Figure 13. The radius of shaft shoulder is 0.8 times than that of the disk. Due to no slip wall boundary condition, the values of v_θ at the outer radius of stator surface and on the surface of shaft shoulder are considered as 0 and 0.8, respectively.

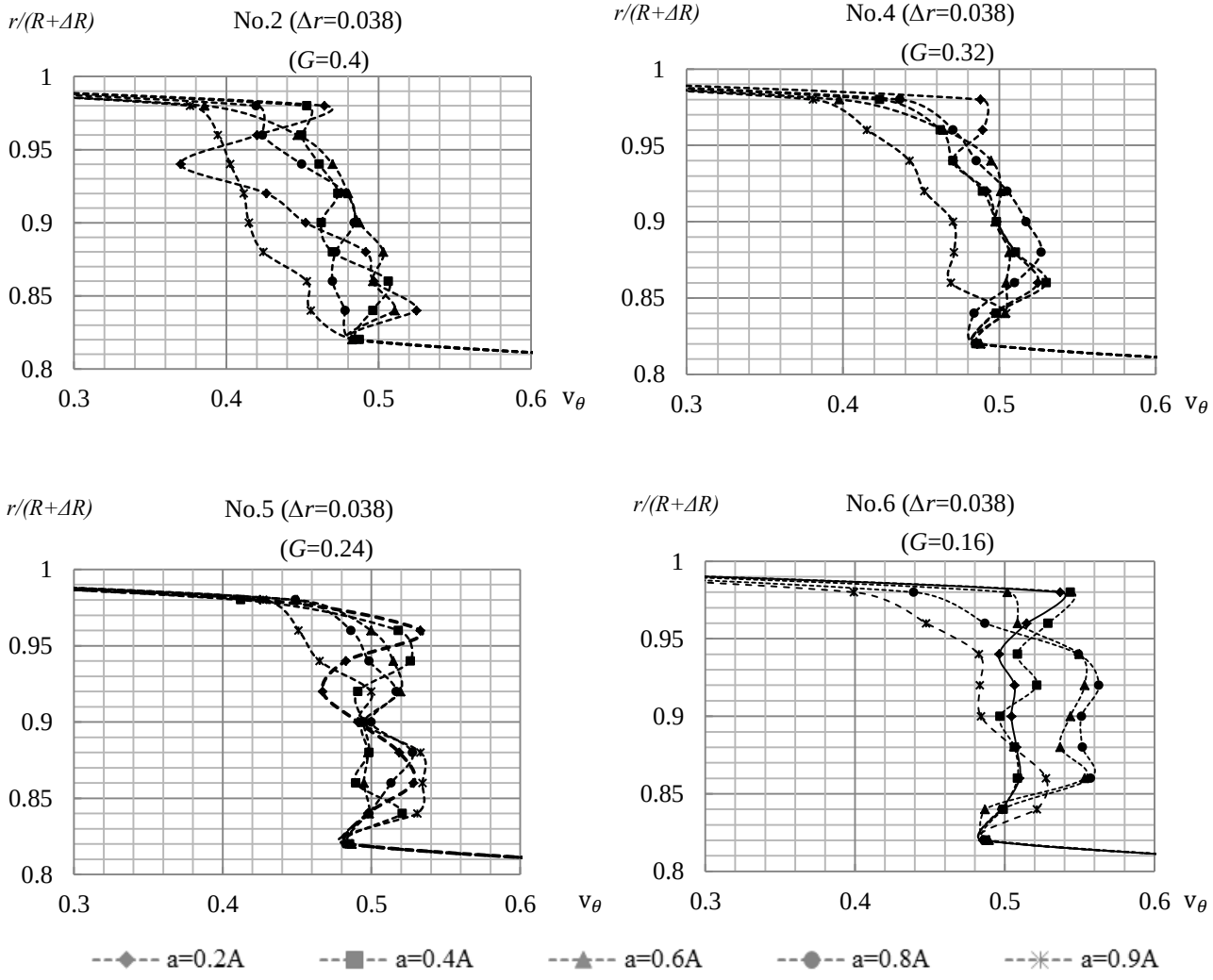

Figure 13: **Distributions of dimensionless tangential velocity**

There is a balance between centrifugal force and pressure gradient. The dimensionless tangential velocity increases with the decrease of axial gap in general. Moving with the conveying fluid, sand is more likely to move radial outward with the increase of v_θ. Due to the axial convection of slurry

from the outer radius of the disk to that of the wall, sand may enter the annular groove. Then, it is quite possible for sand to be discharged along the spiral groove.

The simulation results of the tangential velocity indicate that the axial gap should be minimized.

Distributions of Solid Volume Fraction

The distributions of solid volume fraction, noted as φ_s, are shown in Figure 14.

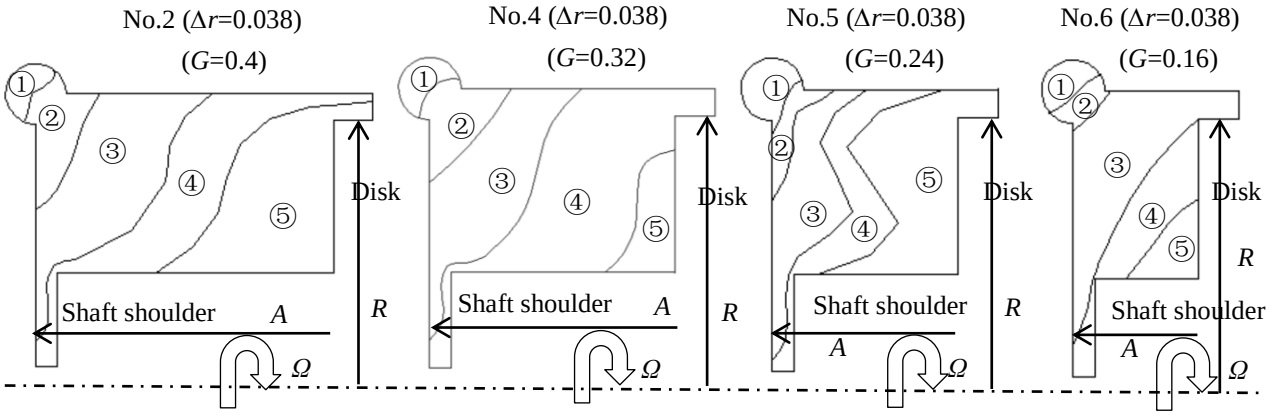

①: φ_s>2%; ②: 1%≤φ_s<2%; ③: 0.5%≤φ_s<1%; ④: 0.2%≤φ_s<0.5%; ⑤: φ_s<0.2%

Figure 14: **Distributions of solid volume fraction**

The highest solid volume fractions are shown in the spiral groove for all case. Relative low solid volume fraction is predicted in No.5. The values of particle concentration in No.6 are higher than that in No.5 in general. Although the values of tangential velocity are higher in No.6 in general (shown in Figure 13), the concentration of sand in the groove is less than that of No.4 and No.5. This results are in accordance with the velocity analyses of No.6. The reason may be that the sand discharge groove and shaft shoulder have large influences on the inner flow. The turbulent flow in No.6 has negative effects on sand exclusion.

TEST RESULTS

In order to further analyze the correctness of the simulation results, the cavity with rear chamber No.5 cavity is produced and tested. The test rig meets the requirements of international B-grade precision (ISO9906-1999). The pump performances are given in Figure 15.

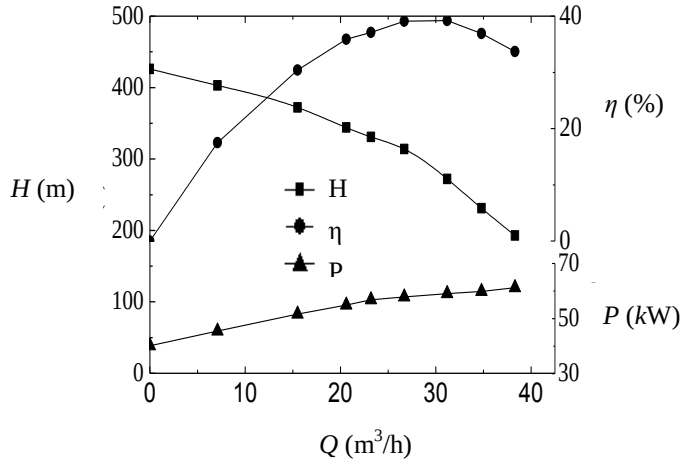

Figure 15: **Pump performances**

The pressure at pump outlet is measured by a pressure transmitter to calculate the pump head,

noted as *H*. The volumetric flow rate of the pump is measured by a turbine flow meter. The speed of rotation is recorded during the experiment. Electric voltage and electric current are monitored to calculate the pump power, noted as *P*. The pump efficiencies, namely η, are calculated based on above results. The density of the slurry is 1160 kg/m^3. The temperature of the slurry is 20℃. This test rig has circulation system at the bottom, which can reduce the settlement of sand. The size of the sand is selected with a screen mesh. During the test, the concentration of sand is measured every 48 hours. Appropriate sand is added to the slurry when the sand concentration decreases more than 20%.

Abrasion test is also accomplished to verify the correctness of sand exclusion. The values of outlet pressure are recorded during the test. When the mechanical seal is broken, large pressure difference contributes to large leakage flow from the rear chamber (approximate 2 Mpa) to the environment. It results in the plunge of pressure head, shown in Figure 16. When p^* (the ratio of p_T to p_0) drops by 10%, the mechanical seal is considered to fail. According to the results, the service life of the SMSP is significantly improved by around 30% after improvement.

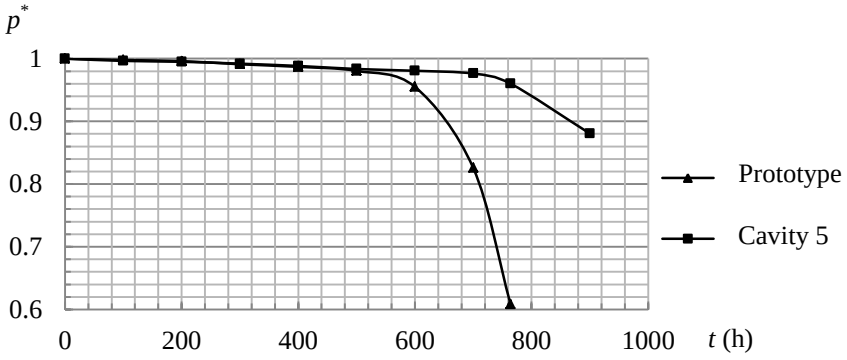

Figure 16: **Results of abrasion tests**

CONCLUSION

Batchelor type flow can be predicted even the flow contains micro-sized sand. Effective sand exclusion can be accomplished based on Batchelor type flow.

Superimposed flow has little influence on the cavity flow when $\Delta r \leqslant 0.038$. Batchelor type flow can be predicted even if the cavity is open and the disk is not infinite.

Since the cavity is designed with a groove, the axial gap should be carefully designed to minimize the influence of groove and shaft shoulder on the cavity flow. When *G* decreases further from 0.24 to 0.16, although the values of v_θ increase, the sand discharge capacity drops obviously. The reason is that the geometries of shaft shoulder and sand discharge groove cannot be ignored for that axial gap. The turbulent flow in the rear chamber makes it hard for sand to enter the groove, which lowers the sand exclusion capacity.

ACKNOWLEDGEMENTS

This study is funded by CSC (China Scholarship Council) and Antai Company.

REFERENCES

Batchelor, G. K., (1951), Note on a class of solutions of the Navier-Stokes equations representing steady rotationally-symmetric flow, The Quarterly Journal of Mechanics and Applied Mathematics, Vol. 4, No. 1, 29-41.

Daily, J. W., Nece, R. E., (1960), Chamber dimension effects on induced flow and frictional resistance of enclosed rotating disks, Journal of Basic Engineering, 82, 217-232.

Debuchy, R., Poncet, S., Abdel Nour, F., Bois, G., (2009), Experimental and Numerical Investigation of Turbulent Air Flow Behavior in a Rotor-Stator Cavity, 8th European

Turbomachinery Conference, Graz, Austria.
Djaoui, M., Malesys, A., Debuchy, R., (1998), Mise en evidence expérimentale de la sensibilité de l'écoulement de type rotorstator aux effets de bord, C. R. Acad. Sci. Paris. t. 327, Série II b, 49-54.
Emmanuel D'Haudt, Stefania Della Gatta, Roger Debuchy, Gerard Bois, Francesco Martelli., (2006), Assessment of experimental and numerical flow investigation in rotating-disc systems, The Eleventh International Symposium on Transport Phenomena and Dynamics of Rotating Machinery, Honolulu, Hawaii, USA.
Kurokawa, J., Sakuma, M., (1988), Flow in a Narrow gap along an Enclosed Rotating Disk with Through-Flow, JSME International Journal, Series II, Vol. 31, No.2, 243-251.
Randriamampianina, A., Elena, L., Fontaine, J. P., Schiestel, R., (1997), Numerical prediction of laminar, transitional and turbulent flows in shrouded rotor-stator systems, Phys. Fluids, 9, 1696-1712.
S. B. Hazra, K. Steiner., (2007), Computation of dilute two-phase flow in a pump, Journal of Computational and Applied Mathematics, 203, 444–460.
Will, B. C., Benra, F.-K., Dohmen, H. J., (2010), Numerical and Experimental Investigation of the Flow in the Side Cavities of a Centrifugal Pump, The 12th International Symposium on Transport Phenomena and Dynamics of Rotating Machinery, ISROMAC13-2009-0002, Honolulu, Hawaii, USA.
Will, B. C., Benra, F.-K., Dohmen, H. J., (2011), Investigation of the Flow in the Side Chambers of a Centrifugal Pump with Volute Casing, 10th International Symposium on Experimental Computational Aerothermodynamics of Internal Flows, Brussels, Belgium.